



# Optimal design of a tunable electromagnetic shunt damper for dynamic vibration absorber<sup>☆,☆☆</sup>

Ruqi Sun, Waion Wong<sup>\*</sup>, Li Cheng

Department of Mechanical Engineering, The Hong Kong Polytechnic University, Hung Hom, Kowloon, 999077, Hong Kong, China

## ARTICLE INFO

### Keywords:

Tunable electromagnetic shunt damper  
Opposing magnets pairs  
Damping coefficient  
Optimum dynamic vibration absorber

## ABSTRACT

Dynamic vibration absorber (DVA) is an effective device for suppressing resonant vibration of noisy machineries and structures. However, the optimum design of DVA requires precise tuning of the damping force in the DVA, which unfortunately is often not practical and prone to changes of working conditions. In this paper, a tunable electromagnetic shunt damper (EMSD) with different opposing magnet pairs configurations is tested for the optimum design of DVA. The optimum magnet pairs configuration is derived to provide the maximum damping force in the DVA. Both simulations and experiments are conducted to verify the damping coefficient variation with the number of magnet pairs in the EMSD. The experimental optimization procedure of the DVA is designed according to the fixed-points theory. The damping force generated by the EMSD can be readily adjusted by varying the external resistance of the EMSD. This is the first experimental implementation report of the optimization procedure described in the fixed-points theory. The proposed tunable EMSD can conveniently allow for onsite optimal tuning of DVA. The proposed design methodology provides fine tuning of the damping coefficient of EMSD to achieve robust optimal DVA performance, even when subject to changes of external parasitic damping.

## 1. Introduction

The theoretical analysis of dynamic vibration absorbers (DVAs) has been the topic with extensive discussions in the literature review. Nishihara [1–3] gave the exact theoretical solution of the  $H_\infty$  optimization tuning based on Den Hartog's classical fixed-points theory [4]. Warburton [5] also developed the exact solution of the  $H_2$  optimization tuning condition for global vibration control. The damping requirement of DVAs were thoroughly analyzed for the optimal working condition of the DVA [6]. The theoretical optimization of DVA was conducted for single degree of freedom (SDOF) vibrating system [7,8] and multi-degree of freedom vibrating system [9,10]. Structural morphing [11–13], different combinations [14] and modified optimization methods [15,16] were proposed for various kinds of vibration control applications. Different types of dynamic vibration absorbers were categorized and the corresponding transfer functions of their dynamic models were compared [17].

Reported applications of DVAs cover both discrete [18] and continuous structures such as beams [19,20] and plates [21,22]. DVAs were also applied in many on-site fields: the vehicle suspension [23], buildings and towers [24,25], machine boring bar [26], micro-

electromechanical systems (MEMS) [27,28], floating raft system [29], pedestrian footbridge [30,31], truss structure [32], high speed rotational machine [33], and piping system [34] etc. The high sensitivity of DVAs to the variation of external conditions has always been a challenging problem, which compromises their performance of DVAs and hinders their wide applications in practice. In particular, the amount of damping in the DVA requires precise tuning to ensure the best effective vibration suppression performance of the controlled structure. Detuned DVA may even amplify the vibration of the controlled structure. Conventional means such as the commonly used fluid viscous damping, for example, is difficult to cope with such a need in terms of providing tunable damping.

Electromagnetic shunt damper (EMSD) was first proposed by Behrens [35] for vibration control with precise tunability of vibration damping. The vibration isolation performance of EMSD is well studied in both linear systems [36] and nonlinear systems [37]. When being applied in the vibration system, the optimal damping resistance is also given to suppress the resonant vibration [38]. With the fine tunability of vibration damping, EMSD is applied in DVA system which requires

<sup>☆</sup> This document is the results of the research project funded by the Research Grant Council of Hong Kong, China for the funding support (Project number: 15206120).

<sup>☆☆</sup> This paper was recommended for publication by Associate Editor Lei Zuo.

<sup>\*</sup> Corresponding author.

E-mail address: [mmwowong@polyu.edu.hk](mailto:mmwowong@polyu.edu.hk) (W. Wong).

precise damping to achieve the system optimal status [39]. A beam-like DVA system is proposed by Kremer with EMSD, both harmonic force [40] and transient [41] excitation in the system are investigated to verify the vibration absorption performance of EMSD.

Moreover, with the capacity of transferring mechanical energy into electrical energy, EMSDs in DVA system always function both in vibration control and energy harvesting. The performance of EMSD simultaneous vibration suppression and energy harvesting function is deeply analyzed in both traditional [42] and beam-like [43] DVA system Galuzzi [44] proposed a rotary shock absorber with EMSD in automotive suspension to harvest energy from road irregularities, and the corresponding experiments verified the damping efficiency performance. The theoretical analysis of EMSD in DVA system with is also conducted to achieve both objectives optimal status [45]. With the aid of micro-controller, the EMSD connected circuit is able to maintain a nearly constant resistance that providing stable damping force [46]. Since the dual-function is performed well, EMSD is widely used in bridge cable [46,47], auto-suspension [44], seat suspension [48], railway transportation [49] for both vibration control and energy harvesting.

Despite the existing work, the structural configuration of EMSD has been seldom investigated in views of improving the electro-mechanical coupling to obtain better damping performance. Existing efforts include the improvement of the EMSD by introducing negative impedance which demands the utilization of external power supply into the system. Behrens [50] first proposed the concept of the negative inductor-resistor for the EMSD shunt circuit. The numerical analysis of EMSD in DVA system shows that, the system response will decrease and the absorbing area will also be broaden with the negative inductance in the shunt circuit [51]. The experimental study of EMSD with negative resistance verified the improved the damping improvement in spacecraft micro-vibration control system [52]. The linear-EMSD and nonlinear-EMSD with negative resistance are both investigated by Yan [53] that giving guidelines to design nonlinear damping.

Inspired by the proven effectiveness of opposing magnet configuration for EMSD performance enhancement [54], this paper presents tunable EMSDs with various opposing magnet pair configurations along the axial direction to improve the damping performance. The damping coefficient of the EMSD peaks when the opposing magnet pairs are properly arranged to strike a balance between the peak radial magnetic flux density and the number of opposing magnets pairs. The EMSD damping peak can be easily searched out with the proposed method below. And the corresponding experimental results verified exist and the accuracy of the peak. The major contribution of this manuscript is: (1) to analyze the effect of system parameters of EMSD with opposing magnet pair configuration on its damping performance and (2) to establish the optimal configuration for this type of EMSD based on the numerical and experimental analysis results such that the damping coefficient of the EMSD can be maximized.

The tunable EMSD empowers the DVA with flexible adaptability to reach and maintain optimal working conditions even when the internal parasitic damping changes by various external factors such as the friction variation of the internal components. As a side benefit, the tunable EMSD also allows for saving energy of the system when working in the higher frequency range exceeding the resonant frequency of the system.

In the following sections, the basic theoretical analysis of EMSD and the classical optimization of DVA through fixed-points theory are introduced first. Subsequently, the EMSDs with various opposing magnets pair configurations are investigated, and the corresponding verifications are conducted through simulation and experiments. Finally, the optimum DVA is implemented and experimentally tested.

## 2. Theoretical basis of EMSD and DVA

### 2.1. Basic concepts and principles of EMSD

The EMSD can be regarded as a linear electric generator, which can potentially be used as an energy harvester. A typical EMSD structure

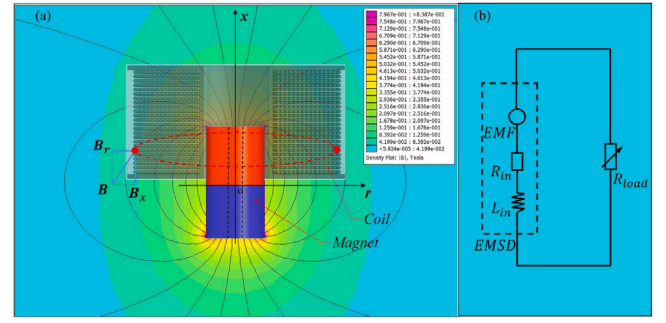


Fig. 1. Typical structure of an EMSD: (a) the magnet and coil, (b) the equivalent coil circuit and external connected tunable resistor.

consists of a magnet and a coil as shown in Fig. 1(a). The motional electromotive force (EMF) is induced between the magnet and the coil by the relative motion. A tunable damping force will then be induced if the two terminals are connected with a variable resistor as shown in Fig. 1(b).

The induced motional EMF,  $\epsilon$ , is measured in volts when the EMSD circuit is open. For the red dashed single loop coil with the red dot  $dl$  in Fig. 1(a), since the relative motion is along the axial direction ( $x$ -axis) under the cylindrical coordinate system, the axial magnetic flux density,  $B_x$ , makes no contribution to the motional EMF. Therefore, only the radial magnetic flux density,  $B_r$ , contributes to the damping function. Therefore, one as

$$\epsilon = - \oint_{loop} B_r(x, r) dl \dot{x} \quad (1)$$

Expressing

$$\epsilon = K_t \dot{x} \quad (2)$$

The transduction factor,  $K_t$ , is defined as

$$K_t = - \oint_{loop} B_r(x, r) dl \quad (3)$$

$K_t$  quantifies the electromechanical coupling strength. In the whole electric coil with  $N$  turns loop as shown in Fig. 1(a),  $K_t$  can be simplified as

$$K_t = -2\pi \sum_{i=1}^N r(i) |B_r(x, r, i)| \quad (4)$$

where  $r$  denotes the radius of the target point.

In the absence of flux leakage and eddy current in the system, if the external resistance  $R_{load}$  is connected with the EMSD coil, the induced damping force  $F_e$  can be expressed as

$$F_e = K_t i = \frac{K_t \epsilon}{Z} \quad (5)$$

where  $i$  is the electric current in the closed circuit and  $Z$  the total circuit impedance which is a tripartite written as

$$|Z| = \sqrt{(R_{in} + R_{load})^2 + (2\pi f L_{in})^2} \quad (6)$$

where  $f$  is the EMF frequency in Hz;  $L_{in}$  the internal inductance of the coil and  $R_{in}$  the internal resistance of the EMSD coil. Since the internal inductance is always very small and the system is mostly applied in low-frequency domain, the inductive impedance can be ignored in most occasions.

Combining Eqs. (2) and (5) yields the damping force as

$$F_e = \frac{K_t^2}{Z} \dot{x} \quad (7)$$

Therefore, the damping coefficient  $c_e$  of the EMSD can be expressed as

$$c_e = \frac{F_e}{\dot{x}} = \frac{K_t^2}{Z} \quad (8)$$

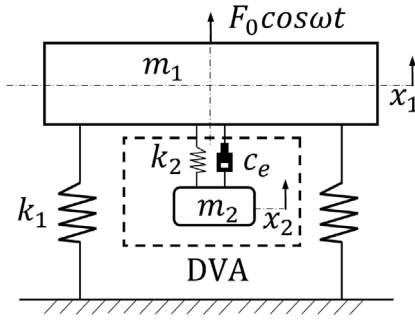


Fig. 2. A vibrating system with DVA.

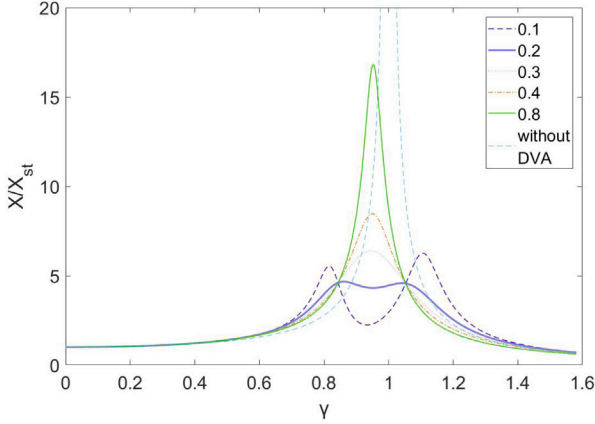


Fig. 3. Displacement amplitude of the primary system with different damping ratios.

## 2.2. Optimization of DVA with the tunable EMSD based on the fixed-points theory

When the EMSD is deployed as a tunable damper, attached to a single-degree-of-freedom vibrating system as shown in Fig. 2, the equations of motion of the system are given by

$$m_1 \ddot{x}_1 + k_1 x_1 + k_2 (x_1 - x_2) + c_e (\dot{x}_1 - \dot{x}_2) = F_0 \cos \omega t \quad (9)$$

$$m_2 \ddot{x}_2 + k_2 (x_2 - x_1) + c_e (\dot{x}_2 - \dot{x}_1) = 0 \quad (10)$$

where  $k_1$ ,  $m_1$  and  $k_2$ ,  $m_2$  denote the spring stiffness and the mass of the primary system and that of the DVA, respectively.  $x_1$  and  $x_2$  denote their respective displacement of the primary system and DVA.  $c_e$  is the equivalent damping coefficient of the EMSD. The natural frequency of the primary system and that of the DVA before they are coupled together can be expressed by  $\omega_{n1} = \sqrt{k_1/m_1}$  and  $\omega_{n2} = \sqrt{k_2/m_2}$ , respectively. The dimensionless displacement  $X_1$  of the primary system can be derived by solving Eqs. (9) and (10) with the fixed points theory [4], giving

$$\frac{X_1}{X_{st}} = \sqrt{\frac{(2\xi\lambda)^2 + (\lambda^2 - \gamma^2)^2}{(2\xi\lambda)^2 [(1+\mu)\lambda^2 - 1]^2 + [\mu\gamma^2\lambda^2 - (\lambda^2 - 1)(\lambda^2 - \gamma^2)]^2}} \quad (11)$$

where  $X_{st} = F_0/k_1$  is the initial static displacement.  $\xi = c_e/c_c$  is the damping ratio.  $c_c = 2m_2\omega_{n1}$  is the critical damping constant of the DVA.  $\lambda = \omega/\omega_{n1}$  is the frequency ratio.  $\gamma = \omega_{n2}/\omega_{n1}$  is the natural frequency ratio, and  $\mu = m_2/m_1$  is the mass ratio. The displacement responses of the primary system with respect to different damping ratios in the frequency domain are shown in Fig. 3 when the mass ratio is 0.1.

As shown in Fig. 3, two fixed points can be observed in the response spectra of the primary system. Moreover, the displacement of the primary mass reaches a min–maximum value at a certain set of frequency

**Table 1**  
Parameters of the magnet and coil.

Magnet	Material	NdFeB N33
	Internal diameter	4 mm
	External diameter	15 mm
	Length	10 mm
	Number	12
Coil	Internal diameter( $d_1$ )	18 mm
	External diameter( $d_2$ )	32 mm
	Total length( $l_c$ )	108 mm
	Turns( $N_{total}$ )	756
	Wire diameter( $d_{wire}$ )	1 mm
	Wire length( $L_{wire}$ )	64 m
	Internal resistance( $R_{in}$ )	1.5075 $\Omega$

ratio and damping ratio value, calculated by [4]

$$\begin{cases} \gamma_{optimal} = \frac{1}{1+\mu} \\ \xi_{optimal} = \sqrt{\frac{3\mu}{8(1+\mu)^3}} \end{cases} \quad (12)$$

Upon a proper design of the EMSD, the optimization of the DVA can be achieved and the tuning procedure is described in the following section.

## 3. Design analyses of EMSD configurations

### 3.1. EMSD with various opposing magnets pairs

Owing to the significantly improved radial magnetic flux density, particularly in the area where the magnet poles are connected, EMSDs with opposing magnets configuration has shown promise in increasing the damping coefficient [54]. With the same amount of magnets and wires, the damping coefficient variation with different opposing magnets pairs configuration needs to be investigated. In this work, twelve ring-shaped magnets, each having a length of 10 mm (as shown in Fig. 1) and an amount to 756 turns with 1 mm wire diameter, are used to construct the EMSDs. Details of the magnet and coil parameters are tabulated in Table 1.

The length of the coil is 12 mm shorter than that of the magnet to provide the skeleton space for winding the coils. Assuming the coil is tightly wound as shown in Fig. 1, the total number of turns  $N_{total}$  is

$$N_{total} = \frac{(r_2 - r_1) l_c}{d_{wire}^2} \quad (13)$$

Then, the total wire length  $L_{wire}$  of the coil can be expressed as

$$L_{wire} = \pi (r_1 + r_2) N_{total} \quad (14)$$

Moreover, the internal resistance can be written as

$$R_{in} = \rho \frac{L_{wire}}{S} = \rho \frac{L_{wire}}{\pi (d_{wire}/2)^2} \quad (15)$$

where  $\rho$  denotes the electrical resistivity of copper and  $S$  the cross-section area of the wire. The calculated results using Eqs. (13) to (15) are shown in Table 1.

Since the number of magnets used is twelve, the value of opposing magnet pairs could be the common divisor of twelve, i.e. 1, 2, 3, 4, 6, and 12. The possible EMSD structures with serial numbers  $M_1$ ,  $M_2$ ,  $M_3$ ,  $M_4$ ,  $M_6$  and  $M_{12}$  are shown in Fig. 4. The twelve magnets are divided into groups depending on the number of the opposing magnets pairs. For  $M_1$  case, the magnets are separated into 2 groups, each containing six magnets. The six magnets are connected in a homodromous direction to form a longer magnet of 60 mm long, then the two longer magnets are tightly connected in opposing direction by a screw through a central 4 mm hole. Other opposing magnets configurations as shown in Fig. 4 follow similar connection rules.

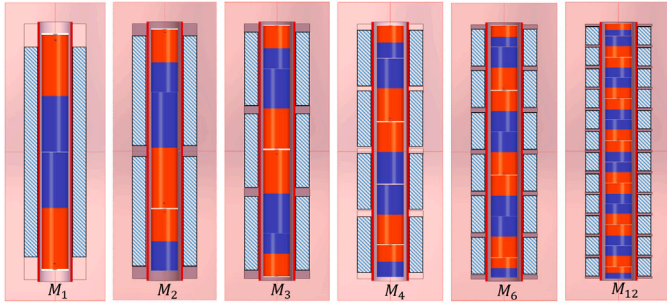


Fig. 4. Structural configuration of EMSDs with different numbers of opposing magnet pairs.

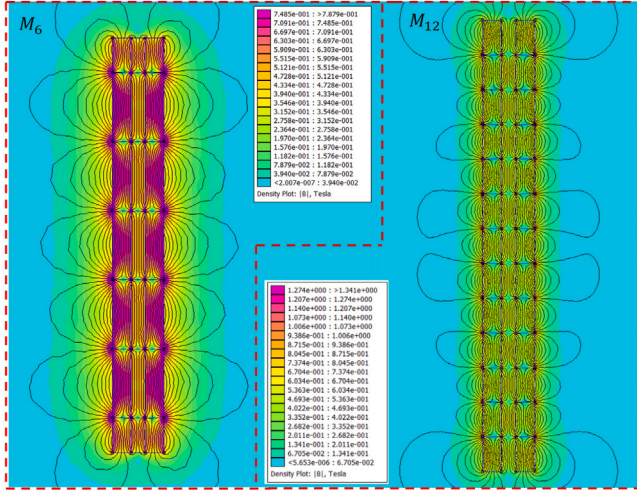


Fig. 5. The magnet flux density of  $M_6$  and  $M_{12}$ , obtained from simulation with the nominal coercivity.

For each adjacent coil pair connected in phase difference with  $M_I$  opposing magnets pairs in Fig. 4, the transduction factor  $K_t$  in Eq. (3) is derived and written as

$$K_t = -2\pi \sum_{j=1}^{M_a} \sum_{i=1}^N r(i, j) |B_r(x, r, i, j)| \quad (16)$$

Since the coil radius  $r(i, j)$  is fixed,  $K_t$  mainly depends on the values and distribution of the radial magnetic flux density  $B_r(x, r)$ .  $B_r(x, r)$  corresponding to different configurations are discussed in the following section.

### 3.2. Analyses on EMSD performance

#### 3.2.1. Radial magnetic flux density

Finite element analysis software FEMM is used to obtain the distribution of  $B_r(x, r)$  around the magnets. FEMM defines the permanent magnet by entering the magnet's coercivity  $H_{cb}$  which can be explained by the current model [55]. According to the standard GB/T 13560-2017 of the sintered NdFeB, the nominal coercivity of the N33 magnet is 876 kA/m and its minimum coercivity is 820 kA/m. However, the actual coercivity of purchased magnets in practice could be lower than the minimum coercivity because of the machining process.

The magnet coercivity  $H_{cb}$  is an important parameter which needs to be calibrated for the accurate data fitting. The peak value of the magnetic flux density, 1 mm above the surface with the  $M_6$  configuration, is measured as 0.9351 T by using a Gaussmeter. However, the corresponding simulation result of the target point is 1.2 T with  $H_{cb}$  as shown in Fig. 5(a), which is very different from the measured

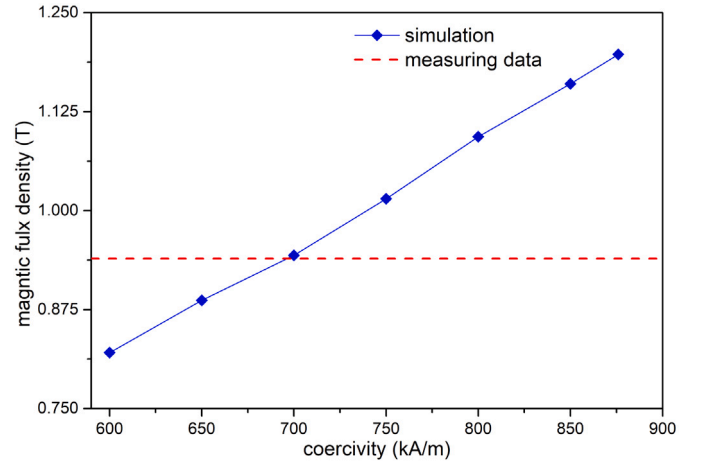


Fig. 6. Surface magnetic flux density of the target point with different coercivity values and the corresponding measuring data.

value. This needs some corrective actions. As shown in Fig. 6, the magnet coercivity is found to be about 700 kA/m by matching the peak value of magnetic flux density 1 mm above the surface with the  $M_6$  configuration between the simulation results and measuring data.

With the ratified  $H_{cb}$ ,  $B_r(x, r)$  variation with the radius and length under different opposing magnet pair configurations are calculated and plotted in Fig. 7. The number of  $B_r(x, r)$  peaks increases with the increase of the number of opposing magnets pair  $M_I$ . The peak values of  $B_r(x, r)$  in Fig. 7 versus the radius  $r$  are plotted in Fig. 8. It shows that the peak of  $B_r(x, r)$  decreases when  $M_I$  increases. As a result, there should exist a certain  $M_I$  at which  $K_t$  becomes maximum.

#### 3.2.2. The transduction factor

With the simulated  $B_r(x, r)$  as shown in Fig. 7, the transduction factors,  $K_t$ , are calculated using Eq. (16) and plotted in Fig. 9 to show its variation with the number of opposing magnets pairs. Both the nominal coercivity and minimum coercivity in production are considered in the  $K_t$  calculations. As shown in Fig. 9,  $K_t$  reaches the maximum at 4 opposing magnets pairs and decreases with the number of opposing magnets pairs further increases. One can conclude that the number of opposing magnets pairs plays a dominant role to  $K_t$  when the pair number is small while the magnetic flux density has a larger effect to  $K_t$  when the pair number is large. Therefore, the maximum  $K_t$  appears in Fig. 9 is a result of the balance between these two factors.

#### 3.2.3. Internal inductance of the coil

The damping coefficient of the EMSD can be obtained with the calculated transduction factor based on Eqs. (6) and (8). The internal resistance  $R_{in}$  can be calculated by considering the whole length of the wire. However, the calculation of the internal inductance  $L_{in}$  is more complicated because of the winding style and the opposing connections in the coils for each magnet pair. Since the adjacent coils are connected with 180° phase difference, the mutual inductance  $M_{ij}$  among the coils needs to be added to the coil inductance while calculating the total internal inductance [56] expressed as

$$L_{in} = \sum_{i=1}^{M_a} L_i \pm 2 \sum_{i=1}^{M_a} \sum_{j=1}^{M_a} M_{ij} \times (1 - \delta_{ij}) \quad (17)$$

where  $\delta_{ij} = 1$  for  $i = j$ , otherwise  $\delta_{ij} = 0$ . The plus-minus sign in Eq. (17) depends on the coil phase difference  $\Delta\phi$  equals to 0° or 180°.  $M_{ij}$  is also multiple summations of the basic mutual inductance of any two single coaxial coils. Taking EMSD with  $M_4$  configuration in Fig. 10(b) as an example, with a coil C1 containing  $T_{C1}$  layers and  $L_{C1}$



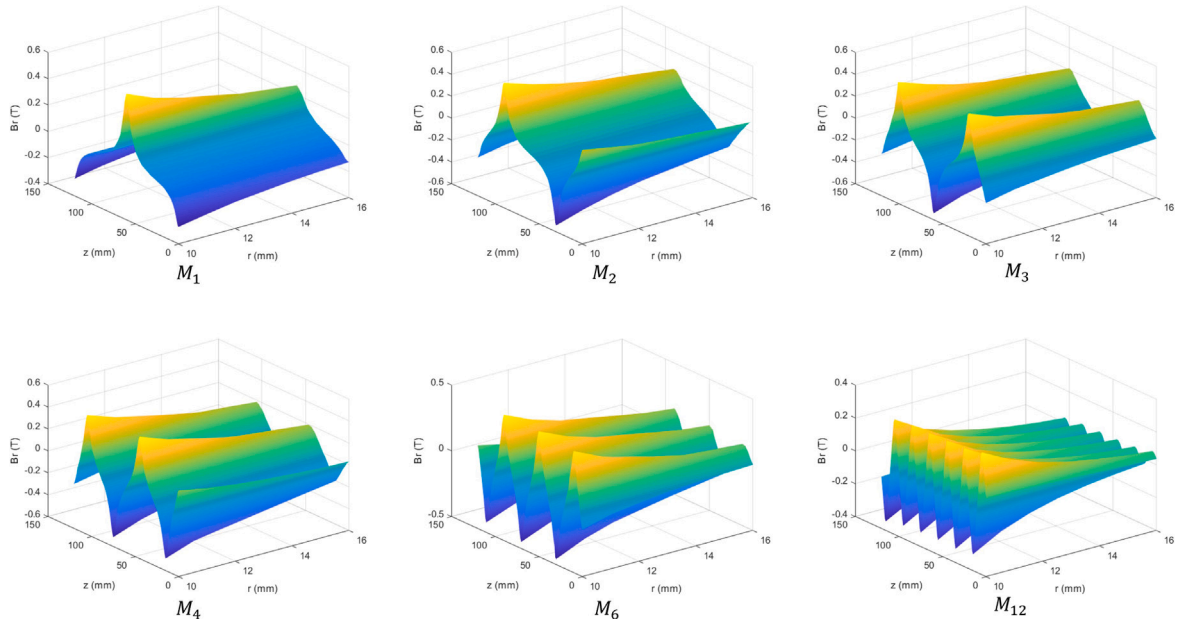


Fig. 7. Radial magnetic flux density of different opposing magnets pairs configurations.

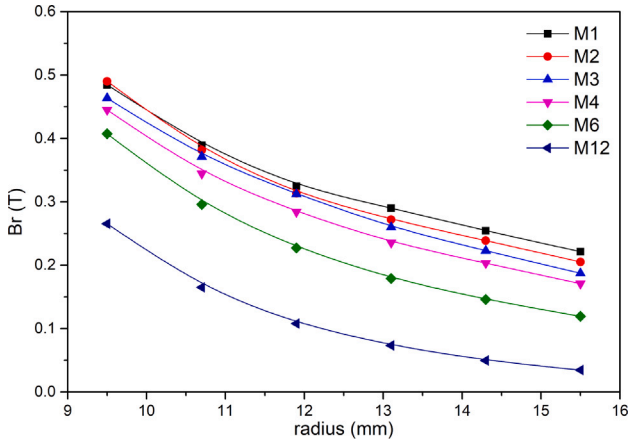


Fig. 8. Radial magnetic flux density variation with radius.

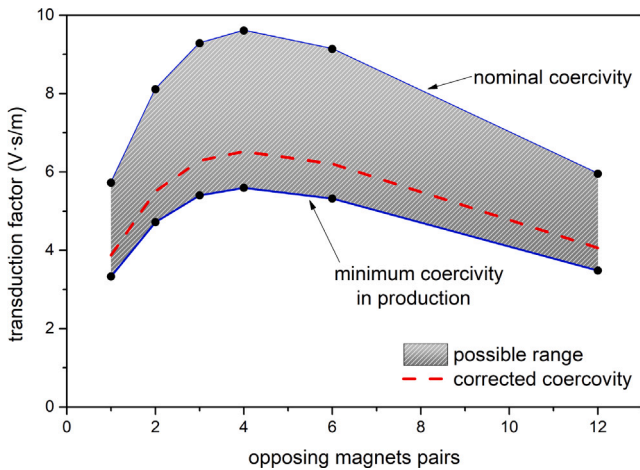


Fig. 9. Transduction factor ( $K_t$ ) variation with the number of opposing magnets pairs.

loops and a coil C2 containing  $T_{C2}$  layers and  $L_{C2}$  loops,  $M_{ij}$  between the two coils can be expressed as

$$M_{12} = \sum_{i=1}^{T_{c1}} \sum_{j=1}^{T_{c1}} \sum_{m=1}^{L_{c1}} \sum_{n=1}^{L_{c2}} M(R_{C1:m}, R_{C2:n}, d_{r(i,j)}) \quad (18)$$

where  $R_{C1:m}$  and  $R_{C2:n}$  are the radius of the  $m$ th loop of C1 and the  $n$ th loop of C2, respectively, and  $d_{r(i,j)}$  denotes the axial distance between the target coils.

Moreover, the basic mutual inductance expression of the two single coaxial coils as shown in Fig. 10(a) could be obtained by the Neumann's formula written as

$$M = \frac{\mu_0}{4\pi} \oint \oint \frac{d\vec{l}_{C1} \times d\vec{l}_{C2}}{R_p} \quad (19)$$

where  $R_p$  is the distance between the vector  $d\vec{l}_{C1}$  and  $d\vec{l}_{C2}$ .

The mutual inductance in Eq. (19) can be rewritten as

$$M = \frac{\mu}{4\pi} \int_0^{2\pi} \int_0^{2\pi} \frac{R_1 R_2 \cos(\varphi_1 - \varphi_2)}{\sqrt{R_1^2 + R_2^2 + d_r^2 - 2R_1 R_2 \cos(\varphi_1 - \varphi_2)}} d\varphi_1 d\varphi_2 \quad (20)$$

For the self-inductance  $L_i$  in Eq. (17), the mutual inductance of the loops for a single layer and the loops of other layers should also be considered since the coil contains  $N_t$  layers and  $N_l$  loops, as shown in Fig. 1a. Taking  $L_1$  as an example, the self-inductance of the coil can be expressed as

$$L_1 = N_t \sum_{i=1}^{N_l} L(R_i, d_{wire}) + 2 \times N_t \sum_{i=1}^{N_l} \sum_{j=1}^{N_l} M(R_i, R_j, 0) \times (1 - \delta_{ij}) + 2 \times \sum_{i=1}^{N_t} \sum_{k=1}^{N_t} \sum_{j=i+1}^{N_l} \sum_{l=1}^{N_l} M(R_k, R_l, d_{ij}) \quad (21)$$

The coil internal inductance can be calculated under different opposing magnet pair configurations as shown in Table 2 based on Eqs. (17)–(21). The internal inductance decreases with the increase of number of opposing magnet pairs. However, in the low frequency range from 10 to 50 Hz, the internal impedance of the coils is not significantly affected by the variations of the internal inductance.

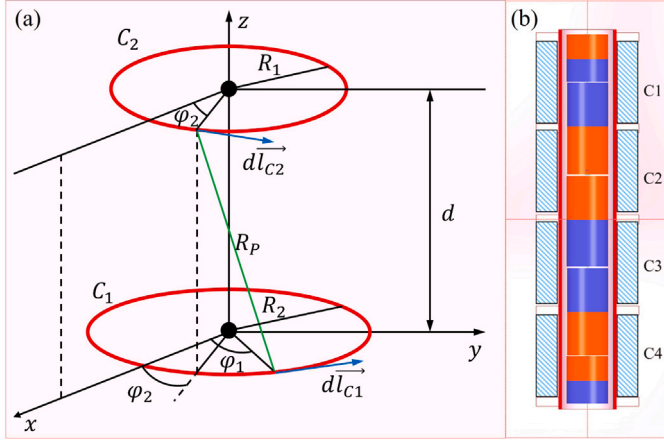


Fig. 10. (a) Model of two single coaxial coils. (b) the  $M_4$  configuration.

**Table 2**  
Calculated results of coil parameters.

	$R_{in} (\Omega)$	$\sum L_i$ (mH)	$\sum M_{ij}$ (mH)	$L_{in}$ (mH)
$M_1$	1.5	2.5738	0	2.5738
$M_2$	1.5	2.3246	-0.0837	2.1571
$M_3$	1.5	2.1142	-0.1598	1.7947
$M_4$	1.5	1.9367	-0.2209	1.4950
$M_6$	1.5	1.6578	-0.2945	1.0687
$M_{12}$	1.5	1.1681	-0.3314	0.5053

### 3.3. Experimental verifications

Experimental tests are conducted to verify the damping coefficient variations of the EMSDs with different configurations predicted in the previous section.

#### 3.3.1. Experimental setup

Three EMSDs,  $M_4$ ,  $M_6$  and  $M_{12}$ , are manufactured and tested for as shown in Fig. 11. The opposing magnets are aligned and fixed following the procedure outlined in Section 3.2. The thickness of the coil spacing board is 3 mm in  $M_4$ , 2 mm in  $M_6$  and 1 mm in  $M_{12}$  configurations respectively. Therefore, the coils of the three EMSDs have the same total length.

The two EMSDs are successively mounted in turn to the vibrating system designed for the DVA test as shown in Fig. 12. Each EMSD has its one end fixed on the floor with a force sensor connected in the middle for damping force measurement while the other end is connected to the vibrating mass. A displacement sensor is fixed on the supporting shelf for the vibration displacement measurement. A non-contact exciter is connected with the B&K 2712 power amplifier to provide a sinusoidal excitation at 10 Hz. The power amplifier and the sensors are all connected to the B&K PULSE 7767 for signal generation and processing.

#### 3.3.2. Damping coefficient measurement

Fig. 13 shows the measured hysteretic loops, whose enclosed area represents the damping capacity of the system. The yellow rectangular loop denotes the unavoidable parasitic damping including friction and air damping in the system. It can be seen that  $M_4$  offers much larger damping than  $M_{12}$  with the same external resistance in the EMSD circuit. The results of  $M_{12}$  is also measured. Since the similarity between  $M_4$  and  $M_6$  except for slight smaller damping tuning range than  $M_6$ , the damping coefficient range of  $M_6$  is only shown in Fig. 15 to avoid the convoluted illustration.

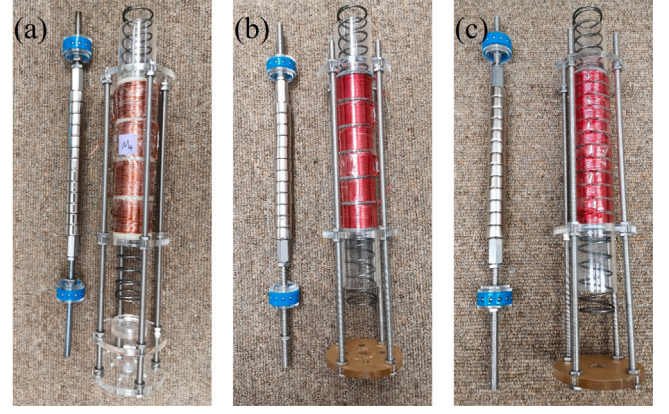


Fig. 11. Three EMSD prototypes with the configurations: (a)  $M_4$ , (b)  $M_6$  and (c)  $M_{12}$ .

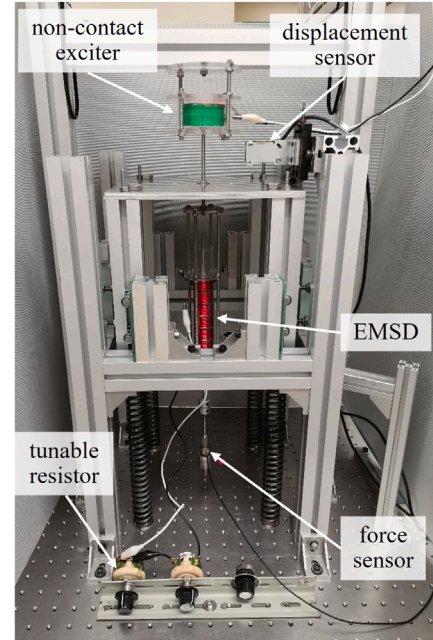


Fig. 12. Experimental setup for EMSD hysteretic loop measurement.

The damping coefficient  $c$  can be determined from the energy lost per cycle expressed as

$$c = \frac{\Delta U}{\pi \omega X^2} = \frac{U_1 - U_0}{2f\pi^2 X^2} \quad (22)$$

where  $\Delta U$  is the energy loss per cycle which can be evaluated by the enclosed area of the hysteretic loop.  $U_1$  denotes the energy lost in the vibration system with a given external resistance in the closed circuit of the EMSD while  $U_0$  denotes the energy loss when the circuit is opened.  $X$  is the displacement amplitude.  $\omega$  and  $f$  are the excitation frequencies in rad/s and Hz, respectively. The calculation yields damping coefficient  $c_e = 15.84$  N s/m for  $M_4$ ,  $c_e = 14.60$  N s/m for  $M_4$  and  $c_e = 5.99$  N s/m for  $M_{12}$  with an external resistance of 1.1  $\Omega$  in the EMSD circuit.

The simulated damping results are compared with the measured ones. The possible range of the transduction factor is shown in Fig. 9. For the coil internal resistance, the calculated result is 1.5  $\Omega$  as shown in Table 1 with the assumption that the coil wires are wound tightly as shown in Fig. 14(a). This results in 7 loops per layer in the skeleton based on the diameter between 18 mm and 32 mm. However, the measured resistances are 1.291  $\Omega$ , 1.305  $\Omega$  and 1.294  $\Omega$  respectively



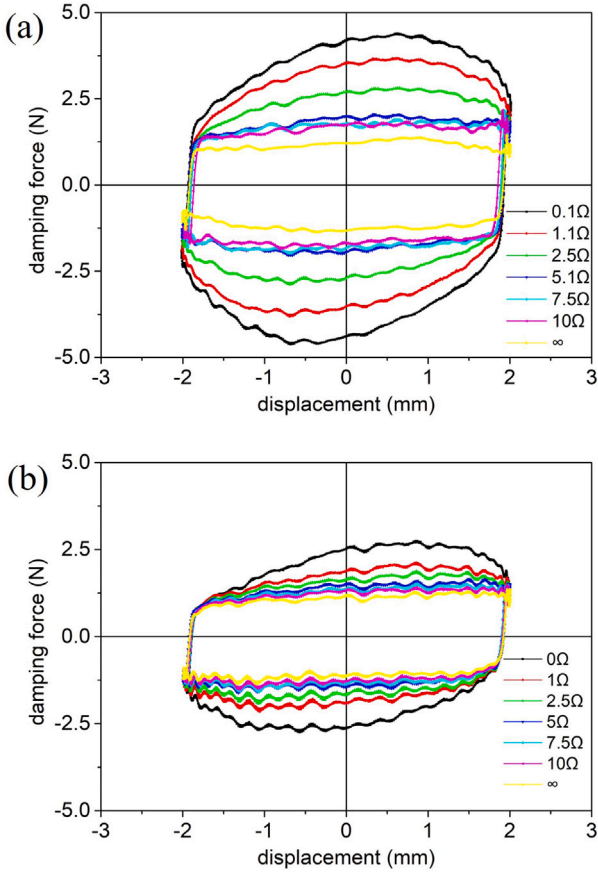


Fig. 13. Hysteretic loops of (a)  $M_4$  and (b)  $M_{12}$ . (For interpretation of the references to color in this figure legend, the reader is referred to the web version of this article.)

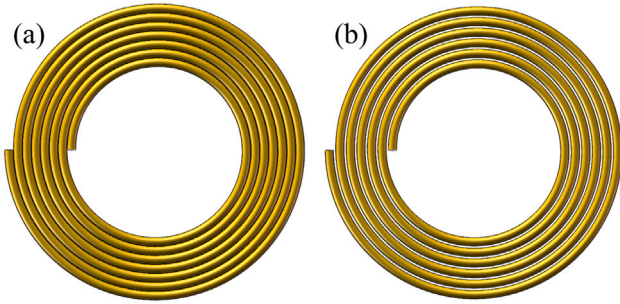


Fig. 14. Top view of the coils with (a) tight winding and (b) loose winding with a 0.2 mm gap.

for  $M_4$ ,  $M_6$  and  $M_{12}$  configurations. The difference suggest that the air gaps exist between the loops as shown in Fig. 14(b), which should be considered. The average value of the measured coil internal resistance is 1.2967  $\Omega$ . Since the coil internal resistance is proportional to the number of turns of coil based on Eqs. (14) and (15), the corrected total turns  $N_{total}$  and the number of loops per layer  $N_l$  are determined as shown in Table 3.

### 3.3.3. Analysis of the test results

With the calibrated coercivity and total number of turns in the coil, the transduction factor can be evaluated based on Eq. (16). The total impedance can be obtained with the measured internal resistance, calculated internal inductance in Section 3.2.3, and the selected external resistance in Section 3.3.2. Then, the simulated damping coefficient

Table 3

Coil parameters comparison between theory and measurements.

	Theoretical data	Corrected theoretical data	Measured data
$R_{in}$	1.5075	1.2921	1.2967
$N_l$	7	6	6
$N_{total}$	756	648	648

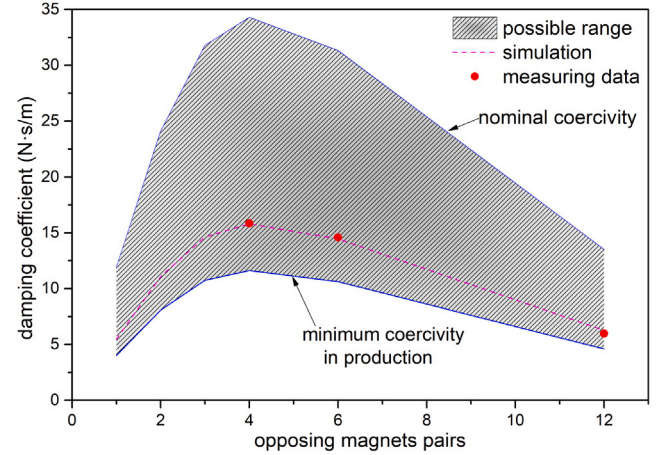


Fig. 15. Comparison of damping coefficient between simulations and experiments.

curve with various configurations is obtained and shown as dashed line in Fig. 15. The three red dots are the measured results for  $M_4$ ,  $M_6$  and  $M_{12}$ . The calculated damping coefficient results agree well with the measured data, which verifies the validity of the EMSD modeling methodology. The hatched zone in Fig. 15 shows the possible damping coefficient due to the variation of different estimated system parameters.

With the increase of number of opposing magnets pairs, the number of the peak values of  $|B_r|$  increases as shown in Fig. 7 while the radial magnetic flux density magnitude  $|B_r|$  induced by opposing magnets configuration decreases as shown in Fig. 8. Therefore, these two counteracting factors on the transduction factor  $K_t$  generate a peak on the curve of  $K_t$  versus number of opposing magnets pairs as shown in Fig. 9. The damping coefficient of the EMSD is related to  $K_t^2$  as shown in Eq. (4). Therefore, there is an optimum number of opposing magnet pairs for achieving the maximum damping coefficient of the EMSD in Fig. 15. This can be obtained with an optimum number of opposing magnet pairs in similar EMSD configurations.

## 4. Experimental optimization of DVA with the tunable EMSD

### 4.1. Experimental setup

Experiments are conducted to test the optimization of the proposed DVA with the tunable EMSD based on the fixed points theory and reported in this section. To the best of our knowledge, this experiment should be the first attempt to conduct on-site optimization of a DVA with a tunable damper based on the fixed-points theory.

The experimental system is built as shown in Fig. 16 to implement the vibration model in Fig. 2. A non-contact electromagnetic exciter on the top provides the driving excitation force with no additional stiffness from the external shaker. A force sensor is mounted below the exciter to monitor the exciting force input to the dynamic system. Two laser displacement sensors are fixed on the supporting holder to monitor the respective displacements of the primary system and the DVA. Four bearings rolling on the smooth glass surface on each side surface to provide a linear guide with minimum friction to the moving parts. The top end of the proposed EMSD coil is rigidly connected

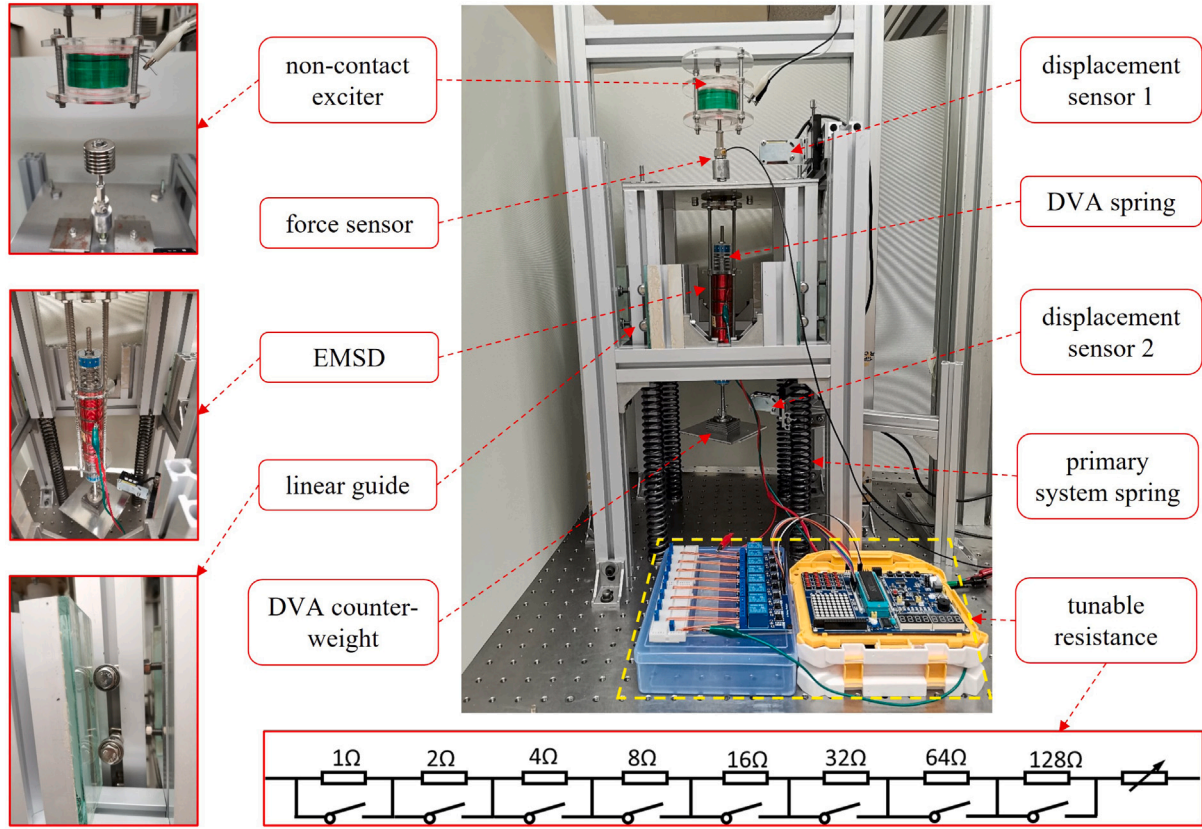


Fig. 16. Experimental setup.

to the primary system. The opposing magnets bar is located in the central hole of the coil skeleton with the pre-compressed DVA spring support. The tunable electrical resistance is implemented with an 8-bit electromagnetic relay as shown in Fig. 16. Moreover, the data acquisition system and signal generation devices are identical to the verification experiment used in Section 3.3.

#### 4.2. DVA parameters calibration

The parameters of an optimum DVA require accurate and meticulous calibration based on the fixed-points theory. In practice, both the frequency and damping ratios can hardly be adjusted on-site to the optimum values because both the stiffness of the spring and the damping of the viscous damper of common DVA are fixed. This is why the application of DVA is limited. In this experiment, the frequency ratio of the DVA is adjusted by changing its mass to achieve the optimum value required by the fixed-points theory. After tuning to the optimum frequency ratio of the DVA, the optimal damping of the DVA is achieved through fine-tuning the electrical resistance of the EMSD circuit.

##### 4.2.1. Parameters identification

According to the fixed-points theory, the optimum frequency ratio  $\gamma$  and damping ratio  $\xi$  in Eq. (12) can be determined once the mass ratio  $\mu$  is fixed. The mass and the stiffness of the primary system are assumed to be fixed. The target mass ratio is firstly set to 0.1 in this experiment, and then the spring stiffness  $k_2$  of the DVA can be determined according to Eq. (12). However, the actual spring stiffness  $k_2$  can hardly match precisely the theoretical result in practice. Therefore, it is more practical to achieve the optimum frequency ratio  $\gamma_{optimal}$  as depicted in Eq. (12) through fine adjustment of the DVA mass  $m_2$ .

The stiffnesses  $k_1$  and  $k_2$  of the selected springs are found through the force and displacement relationship as shown in Fig. 17 from

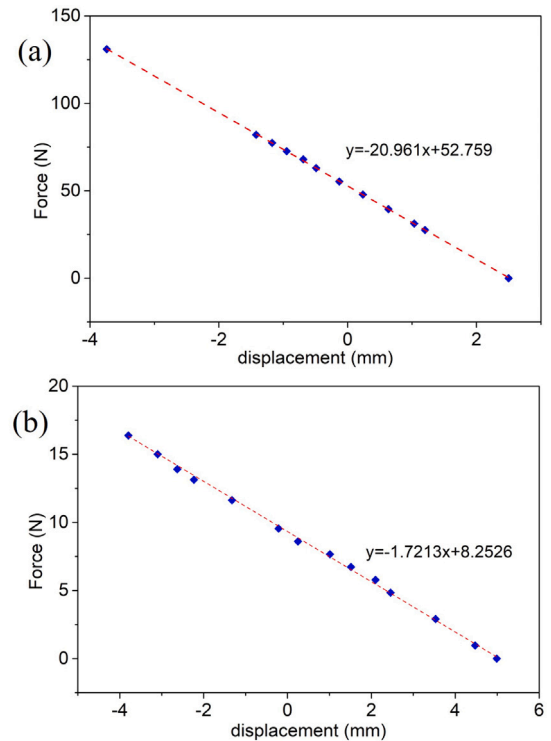


Fig. 17. The spring stiffness determination of (a) primary system and (b) DVA.

compression tests. The blue dots denote the measured data, and the slope of the red dash line gives the spring stiffness obtained from linear



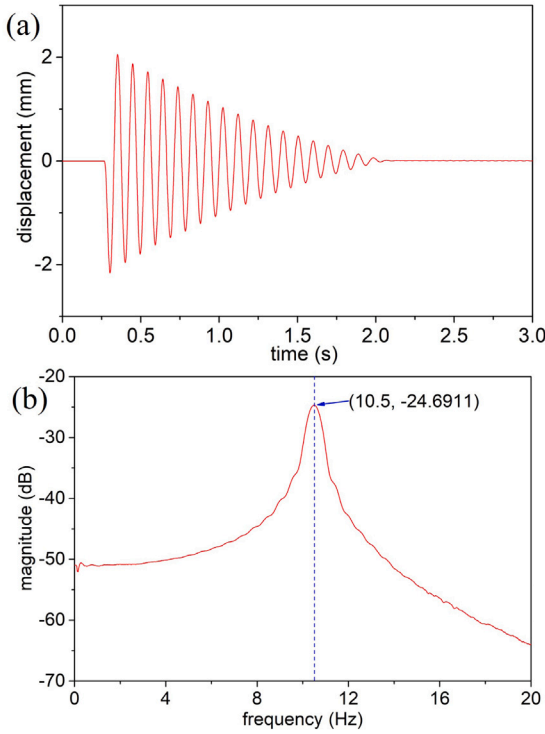


Fig. 18. The free vibration response of the primary system in (a) time domain and (b) frequency domain.

Table 4  
Identified parameters of the experimental system.

Item	Value
$f_{n1}$	10.5 Hz
$f_{n2}$	9.552 Hz
$\gamma$	0.9097
$k_1$	20.961 N/mm
$k_2$	1.7213 N/mm
$m_1$	4.8159 kg
$m_2$	0.4778 kg
$\mu$	0.0992

curve fitting. The measured stiffness of the primary system and that of the DVA are 20.961 N/mm and 1.7213 N/mm, respectively. The target natural frequency is set at around 10 Hz. The mass of coil of the EMSD should be regarded as part of the primary system mass because of the connection between the EMSD and the primary system as shown in Fig. 16. Since the equivalent mass is hard to be measured, the primary system is identified with natural frequency measurement. The obtained natural frequency of the primary system is 10.5 Hz through the real-time frequency domain analysis of the free vibration response as shown in Fig. 18.

With the calibrations above, the parameters of the system are found and listed in Table 4. However, the mass of the DVA still requires fine-tuning to adjust the fixed-points to the same response amplitude in the vibration spectrum of the mass  $m_1$ .

#### 4.2.2. Fixed-points calibration

The frequency ratio  $\gamma$  is firstly tuned to adjust the locations of the two fixed-points P and Q in the response spectrum of mass  $m_1$ , as illustrated in Fig. 19. Since the natural frequency of the primary system  $\omega_{n1}$  and the spring stiffness  $k_2$  of the DVA are fixed, the fixed-points can be tuned by changing the DVA mass  $m_2$  as shown in Fig. 19 so that the response magnitudes of the fixed points P and Q are roughly equal. As shown in Fig. 19, the properly calibrated fixed-points P and Q

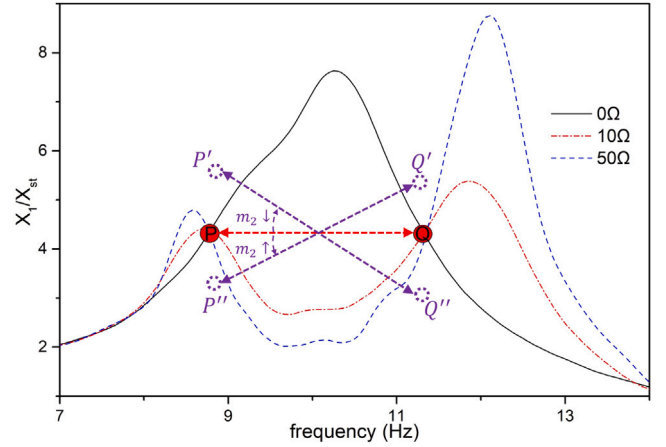


Fig. 19. Calibrated fixed points of the experimental system.

possess the same magnitude of the primary system response when the system is under the swept sinusoidal excitation from 0.1 Hz to 20 Hz with sweeping speed of 1 Hz/s.

The second tuning step is to adjust the damping of the DVA such that the two fixed-points P and Q in Fig. 19 become the highest points of the response spectrum of mass M. Three different values of external resistance are selected and their respective response curves are measured and plotted in Fig. 19. The intersections of the three response curves at different damping show the existence of the fixed points P and Q in Fig. 19. The intersection points are more easily identified with larger differences among the selected external electrical resistances.

#### 4.3. Results analyses

Once the fixed-points are identified and tuned to have equal peaks, the primary system response measurement with different amount of damping can be conducted by changing the external resistance. The measured response spectra of mass M with DVA equipped with EMSDs,  $M_4$  or  $M_{12}$  connected to ten different external resistances are measured and plotted in Fig. 20 respectively. The results show that the optimum DVA is experimentally achieved when the external resistance is 3  $\Omega$  in  $M_4$  and 0.5  $\Omega$  in  $M_{12}$  configuration. The tunability or controllability of the proposed EMSD can provide robustness to the optimal DVA by compensating the detuning effect of the DVA due to any changes of the parameters such as additional friction increases or decreases. The results also show that the EMSD with  $M_4$  configuration possesses a larger damping tunable range than the one with  $M_{12}$  configuration, which also confirms the simulation and test results in Fig. 15.

Moreover, the response of primary mass in higher frequency range above the resonant frequencies is also measured and shown in Fig. 21. It can be seen that the minimum vibration response of the system is obtained with maximum damping when the external resistance is 0  $\Omega$ .

#### 5. Conclusions

An optimum dynamic vibration absorber (DVA) is designed and experimentally implemented with tunable electromagnetic shunt damping (EMSDs) in this paper. The proposed EMSD is composed of opposing magnet pairs with 180° phase difference coils configuration. The design allows damping to be tuned up to its maximum value with a specific number of opposing magnet pairs, verified by both simulations and experiments. In particular, the proposed EMSD design has a twelve magnets configuration which can offer the best damping performance when they are grouped into four opposing magnets pairs. The EMSD is applied to provide tunable damping to a DVA connected to a single degree-of-freedom system. The DVA is tuned experimentally to its

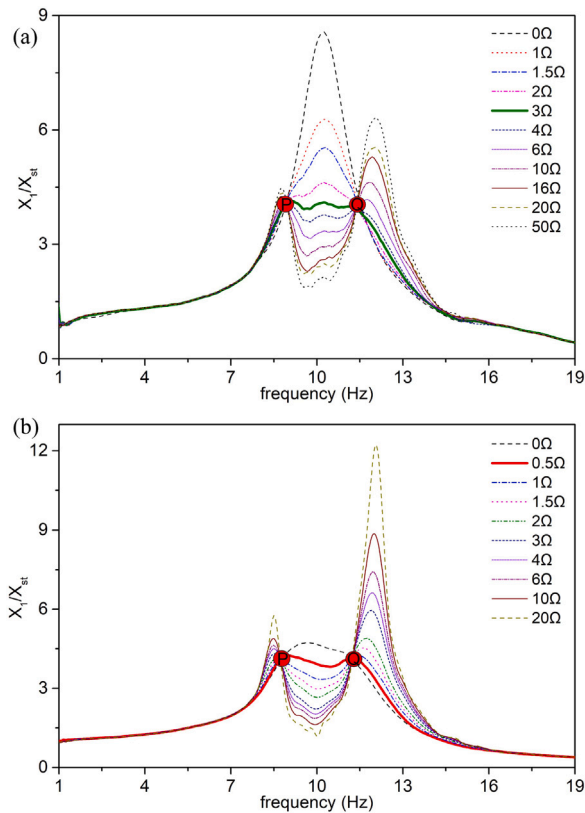


Fig. 20. Primary mass response with different external resistance values of the DVA system with tunable EMSD: (a)  $M_4$ , (b)  $M_{12}$ .

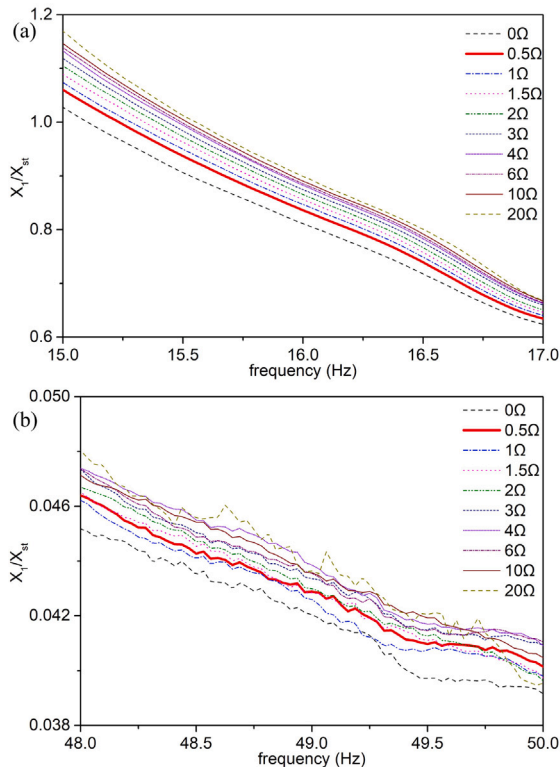


Fig. 21. Primary mass response with different external resistance values in higher frequency domain (a) just crossed the resonant frequency, (b) far away from the resonant frequency; when  $M_{12}$  EMSD is applied in the DVA system.

optimum working condition by using the proposed damper. The tunable EMSDs are shown to be able to uphold the optimal DVA performance even under external disturbances.

### CRediT authorship contribution statement

**Ruqi Sun:** Conceptualization, Methodology, Software, Simulations, Experiments, Writing – original draft, Writing – review & editing. **Waion Wong:** Research proposal, Writing – original draft, Writing – review & editing, Supervision. **Li Cheng:** Review of original draft, Revision, Supervision.

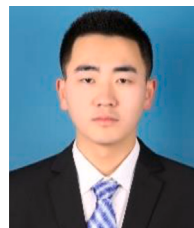
### Declaration of competing interest

The authors declare that they have no known competing financial interests or personal relationships that could have appeared to influence the work reported in this paper.

### References

- [1] Nishihara O, Asami T. Closed-form solutions to the exact optimizations of dynamic vibration absorbers (minimizations of the maximum amplitude magnification factors). *J Vib Acoust* 2002;124(4):576–82. <http://dx.doi.org/10.1115/1.1500335>.
- [2] Nishihara O. Exact optimization of a three-element dynamic vibration absorber: minimization of the maximum amplitude magnification factor. *J Vib Acoust* 2019;141(1):011001. <http://dx.doi.org/10.1115/1.4040575>.
- [3] Asami T, Nishihara O. Closed-form exact solution to  $H_\infty$  optimization of dynamic vibration absorbers (application to different transfer functions and damping systems). *J Vib Acoust* 2003;125(3):398–405. <http://dx.doi.org/10.1115/1.1569514>.
- [4] Den Hartog JP. *Mechanical vibrations*. Courier Corporation; 1985.
- [5] Warburton G. Optimum absorber parameters for minimizing vibration response. *Earthq Eng Struct D* 1981;9(3):251–62. <http://dx.doi.org/10.1002/eqe.4290090306>.
- [6] Krenk S. Frequency analysis of the tuned mass damper. *J Appl Mech* 2005;72(6):936–42. <http://dx.doi.org/10.1115/1.2062867>.
- [7] Asami T, Nishihara O, Baz AM. Analytical solutions to  $H_\infty$  and  $H_2$  optimization of dynamic vibration absorbers attached to damped linear systems. *J Vib Acoust* 2002;124(2):284–95. <http://dx.doi.org/10.1115/1.1456458>.
- [8] Asami T, Nishihara O. Closed-form exact solution to  $H_\infty$  optimization of dynamic vibration absorbers (application to different transfer functions and damping systems). *J Vib Acoust* 2003;125(3):398–405. <http://dx.doi.org/10.1115/1.1569514>.
- [9] Wong W, Cheung Y. Optimal design of a damped dynamic vibration absorber for vibration control of structure excited by ground motion. *Eng Struct* 2008;30(1):282–6. <http://dx.doi.org/10.1016/j.engstruct.2007.03.007>.
- [10] Cheung Y, Wong W.  $H_\infty$  and  $H_2$  optimizations of a dynamic vibration absorber for suppressing vibrations in plates. *J Sound Vib* 2009;320(1–2):29–42. <http://dx.doi.org/10.1016/j.jsv.2008.07.024>.
- [11] Shen Y, Xing Z, Yang S, Sun J. Parameters optimization for a novel dynamic vibration absorber. *Mech Syst Signal Pr* 2019;133:106282. <http://dx.doi.org/10.1016/j.ymssp.2019.106282>.
- [12] Cheung Y, Wong W. Design of a non-traditional dynamic vibration absorber. *Journal Acoust Soc Am* 2009;126(2):564–7. <http://dx.doi.org/10.1121/1.3158917>.
- [13] Cheung Y, Wong W.  $H_2$  Optimization of a non-traditional dynamic vibration absorber for vibration control of structures under random force excitation. *J Sound Vib* 2011;330(6):1039–44. <http://dx.doi.org/10.1016/j.jsv.2010.10.031>.
- [14] Asami T. Optimal design of double-mass dynamic vibration absorbers arranged in series or in parallel. *J Vib Acoust* 2017;139(1). <http://dx.doi.org/10.1115/1.4034776>.
- [15] Viana FAC, Kotinda GI, Rade DA, Steffen Jr V. Tuning dynamic vibration absorbers by using ant colony optimization. *Comput Struct* 2008;86(13–14):1539–49. <http://dx.doi.org/10.1016/j.compstruc.2007.05.009>.
- [16] Wong W, Fan R, Cheng F. Design optimization of a viscoelastic dynamic vibration absorber using a modified fixed-points theory. *Journal Acoust Soc Am* 2018;143(2):1064–75. <http://dx.doi.org/10.1121/1.5024506>.
- [17] Cheung Y, Wong W, Cheng L. A subsystem approach for analysis of dynamic vibration absorbers suppressing broadband vibration. *J Sound Vib* 2015;342:75–89. <http://dx.doi.org/10.1016/j.jsv.2014.12.039>.
- [18] Komatsuzaki T, Inoue T, Terashima O. Broadband vibration control of a structure by using a magnetorheological elastomer-based tuned dynamic absorber. *Mechatronics* 2016;40:128–36. <http://dx.doi.org/10.1016/j.mechatronics.2016.09.006>.

- [19] Wong W, Tang S, Cheung Y, Cheng L. Design of a dynamic vibration absorber for vibration isolation of beams under point or distributed loading. *J Sound Vib* 2007;301(3–5):898–908. <http://dx.doi.org/10.1016/j.jsv.2006.10.028>.
- [20] Hua Y, Wong W, Cheng L. Optimal design of a beam-based dynamic vibration absorber using fixed-points theory. *J Sound Vib* 2018;421:111–31. <http://dx.doi.org/10.1016/j.jsv.2018.01.058>.
- [21] Verbaan C, Rosielle P, Steinbuch M. Broadband damping of non-rigid-body resonances of planar positioning stages by tuned mass dampers. *Mechatronics* 2014;24(6):712–23. <http://dx.doi.org/10.1016/j.mechatronics.2013.12.013>.
- [22] Cheung Y, Wong W.  $H_\infty$  And  $H_2$  optimizations of a dynamic vibration absorber for suppressing vibrations in plates. *J Sound Vib* 2009;320(1–2):29–42. <http://dx.doi.org/10.1016/j.jsv.2008.07.024>.
- [23] Shen Y, Chen L, Yang X, Shi D, Yang J. Improved design of dynamic vibration absorber by using the inerter and its application in vehicle suspension. *J Sound Vib* 2016;361:148–58. <http://dx.doi.org/10.1016/j.jsv.2015.06.045>.
- [24] Soto MG, Adeli H. Tuned mass dampers. *Arch Comput Method E* 2013;20(4):419–31. <http://dx.doi.org/10.1007/s11831-013-9091-7>.
- [25] Zhan W, Cui Y, Feng Z, Cheung K, Lam J, Gao H. Joint optimization approach to building vibration control via multiple active tuned mass dampers. *Mechatronics* 2013;23(3):355–68. <http://dx.doi.org/10.1016/j.mechatronics.2013.01.012>.
- [26] Rubio L, Loya J, Miguélez M, Fernández-Sáez J. Optimization of passive vibration absorbers to reduce chatter in boring. *Mech Syst Signal Pr* 2013;41(1–2):691–704. <http://dx.doi.org/10.1016/j.ymssp.2013.07.019>.
- [27] Diveyev B, Kernyskiy I, Kolisnyk K, Pasternak M, Sava R. Optimization of dynamic vibration absorbers for mems. In: *Perspective technologies and methods in MEMS design*. IEEE; 2011, p. 37–9.
- [28] Sapiński B, Jastrzębski Ł, Góldasz J. Electrical harmonic oscillator with MR damper and energy harvester operating as TMD: Experimental study. *Mechatronics* 2020;66:102324. <http://dx.doi.org/10.1016/j.mechatronics.2020.102324>.
- [29] Sun H, Zhang K, Zhang P, Chen H. Application of dynamic vibration absorbers in floating raft system. *Appl Acoust* 2010;71(3):250–7. <http://dx.doi.org/10.1016/j.apacoust.2009.09.005>.
- [30] Fujino Y, Siringoringo D. Vibration mechanisms and controls of long-span bridges: a review. *Struct Eng Int* 2013;23(3):248–68. <http://dx.doi.org/10.2749/101686613X13439149156886>.
- [31] Santos FA, Nunes J. Toward an adaptive vibration absorber using shape-memory alloys, for civil engineering applications. *J Intel Mat Syst Str* 2018;29(5):729–40. <http://dx.doi.org/10.1177/1045389X17721031>.
- [32] Yamada S, Nambu Y, Chiba M. Implementation and application of digitally controlled piezoelectric vibration absorbers to truss structures. *Acta Astronaut* 2019;156:70–7. <http://dx.doi.org/10.1016/j.actaastro.2018.05.052>.
- [33] Xiang B, Wang W. Electromagnetic vibration absorber for torsional vibration in high speed rotational machine. *Mech Syst Signal Pr* 2020;140:106639. <http://dx.doi.org/10.1016/j.ymssp.2020.106639>.
- [34] Mani Y, Senthilkumar M. Shape memory alloy-based adaptive-passive dynamic vibration absorber for vibration control in piping applications. *J Vib Control* 2015;21(9):1838–47. <http://dx.doi.org/10.1177/1077546313492183>.
- [35] Behrens S, Fleming AJ, Moheimani SOR. Electromagnetic shunt damping. In: *Proceedings 2003 IEEE/ASME international conference on advanced intelligent mechatronics (AIM 2003)*, Vol. 2. IEEE; 2003, p. 1145–50. <http://dx.doi.org/10.1109/AIM.2003.1225504>.
- [36] Behrens S, Fleming AJ, Moheimani SOR. Vibration isolation using a shunted electromagnetic transducer. In: *Smart structures and materials 2004: damping and isolation*, Vol. 5386. International Society for Optics and Photonics; 2004, p. 506–15. <http://dx.doi.org/10.1117/12.539690>.
- [37] Ma H, Yan B, Zhang L, Zheng W, Wang P, Wu C. On the design of nonlinear damping with electromagnetic shunt damping. *Int J Mech Sci* 2020;175:105513. <http://dx.doi.org/10.1016/j.ijmecsci.2020.105513>.
- [38] Behrens S, Fleming AJ, Moheimani SOR. Passive vibration control via electromagnetic shunt damping. *IEEE/ASME T Mech* 2005;10(1):118–22. <http://dx.doi.org/10.1109/TMECH.2004.835341>.
- [39] Ikegame T, Takagi K, Inoue T. Exact solutions to  $H_\infty$  and  $H_2$  optimizations of passive resonant shunt circuit for electromagnetic or piezoelectric shunt damper. *J Vib Acoust* 2019;141(3). <http://dx.doi.org/10.1115/1.4042819>.
- [40] Kremer D, Liu K. A nonlinear energy sink with an energy harvester: harmonically forced responses. *J Sound Vib* 2017;410:287–302. <http://dx.doi.org/10.1016/j.jsv.2017.08.042>.
- [41] Kremer D, Liu K. A nonlinear energy sink with an energy harvester: transient responses. *J Sound Vib* 2014;333(20):4859–80. <http://dx.doi.org/10.1016/j.jsv.2014.05.010>.
- [42] Zuo L, Cui W. Dual-functional energy-harvesting and vibration control: electromagnetic resonant shunt series tuned mass dampers. *J Vib Acoust* 2013;135(5). <http://dx.doi.org/10.1115/1.4024095>.
- [43] Yuan M, Liu K, Sadhu A. Simultaneous vibration suppression and energy harvesting with a non-traditional vibration absorber. *J Intel Mat Syst Struct* 2018;29(8):1748–63. <http://dx.doi.org/10.1177/1045389X17754263>.
- [44] Galluzzi R, Circosta S, Amati N, Tonoli A. Rotary regenerative shock absorbers for automotive suspensions. *Mechatronics* 2021;77:102580. <http://dx.doi.org/10.1016/j.mechatronics.2021.102580>.
- [45] Cai Q, Zhu S, Ke S. Can we unify vibration control and energy harvesting objectives in energy regenerative tuned mass dampers? *Smart Mater Struct* 2020;29(8):087002. <http://dx.doi.org/10.1088/1361-665X/ab92de>.
- [46] Cai Q, Zhu S. Enhancing the performance of electromagnetic damper cum energy harvester using microcontroller: Concept and experiment validation. *Mech Syst Signal Pr* 2019;134:106339. <http://dx.doi.org/10.1016/j.ymssp.2019.106339>.
- [47] Zhu S, Shen W, Xu Y. Linear electromagnetic devices for vibration damping and energy harvesting: Modeling and testing. *Eng Struct* 2012;34:198–212. <http://dx.doi.org/10.1016/j.engstruct.2011.09.024>.
- [48] Xia X, Zheng M, Liu P, Zhang N, Ning D, Du H. Friction observer-based hybrid controller for a seat suspension with semi-active electromagnetic damper. *Mechatronics* 2021;76:102568. <http://dx.doi.org/10.1016/j.mechatronics.2021.102568>.
- [49] Lin T, Wang JJ, Zuo L. Efficient electromagnetic energy harvester for rail-road transportation. *Mechatronics* 2018;53:277–86. <http://dx.doi.org/10.1016/j.mechatronics.2018.06.019>.
- [50] Behrens S, Fleming AJ, Moheimani SOR. Negative inductor-resistor controller for electromagnetic shunt Damping1. *IFAC Proc Vol* 2004;37(14):429–34. [http://dx.doi.org/10.1016/S1474-6670\(17\)31142-4](http://dx.doi.org/10.1016/S1474-6670(17)31142-4).
- [51] Zhou S, Jean-Mistral C, Chesné S. Electromagnetic shunt damping with negative impedances: optimization and analysis. *J Sound Vib* 2019;445:188–203. <http://dx.doi.org/10.1016/j.jsv.2019.01.014>.
- [52] Stabile A, Aglietti GS, Richardson G, Smet G. Design and verification of a negative resistance electromagnetic shunt damper for spacecraft micro-vibration. *J Sound Vib* 2017;386:38–49. <http://dx.doi.org/10.1016/j.jsv.2016.09.024>.
- [53] Yan B, Ma H, Yu N, Zhang L, Wu C. Theoretical modeling and experimental analysis of nonlinear electromagnetic shunt damping. *J Sound Vib* 2020;471:115184. <http://dx.doi.org/10.1016/j.jsv.2020.115184>.
- [54] Sun R, Wong W, Cheng L. Tunable electromagnetic shunt damper with opposing magnets configuration. *Smart Mater Struct* 2020;29(11):115034. <http://dx.doi.org/10.1088/1361-665X/abb21d>.
- [55] Furlani EP. *Permanent magnet and electromechanical devices: materials, analysis, and applications*. Academic Press; 2001.
- [56] Khan SR, Pavuluri SK, Desmulliez MPY. Accurate modeling of coil inductance for near-field wireless power transfer. *IEEE Trans Microw Theory* 2018;66(9):4158–69. <http://dx.doi.org/10.1109/TMTT.2018.2854190>.



**Ruqi Sun** received his B.S. degree in vehicle engineering and M.Sc. degree in mechanical engineering from China University of Petroleum (East China), Qingdao, China, in 2014 and 2017. He is currently pursuing his Ph.D. degree on vibration control with tunable damping at The Hong Kong Polytechnic University. His research interests include vibration control, smart structures, energy harvesting, and electromagnetic transducers.



**Waion Wong** received his Ph.D. degree in mechanical engineering from The Hong Kong Polytechnic University, Hong Kong, in 1997. From 1990 to 1999, he worked as a lecturer at the Hong Kong Polytechnic University. He is currently working as an associate professor at The Hong Kong Polytechnic University. His research interests are vibration analysis and control, laser diagnostics and signal processing.



**Li Cheng** received his Ph.D. degree in mechanical engineering from the Institut National des Sciences Appliquées de Lyon (INSA-Lyon), Lyon, France, in 1989. He is currently a Chair Professor and Director of Consortium for Sound and Vibration Research (CSVSR) at the Department of Mechanical Engineering, PolyU. He has authored more than 500 peer-reviewed journal and conference articles. His research interests mainly cover noise and vibration control, smart materials and structures, fluid-structure interaction, and damage detection.